

See discussions, stats, and author profiles for this publication at: <https://www.researchgate.net/publication/320213955>

Hypersonic flow past nose cones of different geometries: a comparative study

Article in SIMULATION: Transactions of The Society for Modeling and Simulation International · October 2017

DOI: 10.1177/0037549717733051

CITATIONS

16

READS

11,196

3 authors:



Ashish Narayan

Kolhan University

16 PUBLICATIONS 115 CITATIONS

[SEE PROFILE](#)



Narayanan Subramanian

University of Southampton

51 PUBLICATIONS 784 CITATIONS

[SEE PROFILE](#)



Rakesh Kumar

Indian Institute of Technology (ISM) Dhanbad

81 PUBLICATIONS 483 CITATIONS

[SEE PROFILE](#)

Some of the authors of this publication are also working on these related projects:



Deepak Kumar Mandal's Lab [View project](#)



Numerical Simulations of Heat Transfer Enhancement in Flowing Nanofluids [View project](#)



Hypersonic flow past nose cones of different geometries: a comparative study

Ashish Narayan, S Narayanan and Rakesh Kumar

Abstract

The present work provides a detailed comparative study of the hypersonic flow past spherically blunted and parabolic nose cones at a Mach number of 5.8, numerically. The main focus of the paper is to determine the geometry and parameters of the nose cones that provide minimum aerodynamic drag and heating. Studies on spherically blunted and parabolic nose cones are performed for different fineness ratios at zero angle of attack. It is observed that for fineness ratio <1.2 , blunted cones provide minimum drag, whereas at higher values of fineness ratios >1.2 , parabolic nose cones provide superior drag reduction. Detailed comparison of the flow/shock features in the vicinity of the blunted and parabolic nose cones for different fineness ratios is also shown in order to determine its influence on aerodynamic drag. An empirical correlation developed for the total drag coefficient based on regression analysis for a parabolic nose cone reveals that it is mainly a function of the maximum pressure coefficient and fineness ratio. In general, the present study reveals that parabolic nose cones at higher fineness ratios are preferred over spherically blunted ones for achieving higher drag reductions and lower heating in hypervelocity vehicles.

Keywords

Spherically blunted nose cone, parabolic nose cone, aerodynamic drag coefficient, heat flux

I. Introduction

In the design of high speed aerodynamic vehicles (i.e., entry vehicles) such as missiles, rockets, space shuttles, etc., different nose shapes are used for reducing the aerodynamic drag in order to enhance its performance. The present study concentrates on investigating different nose cone shapes (i.e., spherically blunted nose cones and parabolic nose cones) with different parameters on the flow/shock characteristics, such as the shape of the shock wave near the nose, shock detachment distance, etc., in order to determine the nose cone geometry and parameters that provide minimum aerodynamic drag, since drag reduction is essential for the better performance of the hypervelocity vehicles. The formation of bow shock formed in the vicinity of the nose, shock detachment distance, shock layer, flow turning angle, etc., play a substantial role in modifying the aerodynamic characteristic for achieving better performance in nose cones. Even though several studies have been done on flow past different nose cones at hypersonic Mach numbers, detailed numerical investigation of spherically blunted and parabolic nose cones for different fineness ratios on the aerodynamic characteristics, such as

drag, shock detachment distance, heating, etc., is scarce, which forms the specific objective of the present study. Thus, a detailed numerical simulation is carried out in the current study to predict the aerodynamic drag as well as heating characteristics of spherically blunted and parabolic nose cones of different configurations for determining the influence of geometry and fineness ratios on aerodynamic drag and heating. Due to the unavailability of literatures on hypersonic flow past parabolic nose cones, some of the relevant literatures on spherically blunted nose cones are given below:

O'Bryant¹ experimentally investigated the effect of different bluntness ratios and semi-cone angles on the aerodynamic characteristics of the hypersonic flow past a

Department of Mechanical Engineering, Indian Institute of Technology (Indian School of Mines), India

Corresponding author:

S Narayanan, Assistant Professor, Department of Mechanical Engineering, Indian Institute of Technology (Indian School of Mines), Dhanbad-826004, Jharkhand, India.
Email: snarayan.1979@gmail.com

spherically blunted nose cone. He found the existence of pressure minimum instantaneously downstream of the nose-cone junction for a semi-cone angle of 40° , whereas it is positioned far downstream for a smaller semi-cone angle of 20° . It was observed that the shock detachment distance between the bow shock and the blunted nose cone surface varies linearly with the nose radius.

Menezes et al.² experimentally investigated the effect of a multi step base on the overall drag characteristics of a missile-shaped body with a flat base configuration, at a hypersonic Mach number of 5.75. It was observed that the after body with a multi step base showed about 8% reduction in the overall drag as compared to the flat base configuration.

Arsalan et al.³ numerically investigated the effects of bluntness ratios on the aerodynamic characteristics of spherically blunted cones with different semi-cone angles and orientations. They observed that the effects of the bluntness ratio on the aerodynamic performances are negligible for large semi-cone angle geometries as compared to the smaller ones.

Owens⁴ experimentally studied the effect of bluntness ratios on the aerodynamic characteristics of the nose cones for the range of Mach numbers from 0.5 to 5. It was observed that at higher Mach numbers, the effects of bluntness on the aerodynamic characteristics, such as normal force coefficient, fore body drag coefficient, etc., were significant for the smaller semi-cone angles, whereas they are insignificant for the larger ones. He noticed that for semi-cone angles less than 30° , the locations of the center of pressure are more sensitive to bluntness than the Mach number, but for those with a semi-cone angle greater than 35° , the center of pressure is positioned downstream of the base and is influenced by Mach number changes and bluntness.

Perkins et al.⁵ measured the drag and pressure distribution on a series of hemispherical blunted nose cones at zero angle of attack for the range of Mach numbers and Reynolds numbers from 1.24 to 7.4 and 1.0×10^6 to 7.5×10^6 . They found that the diameter of the hemispherical tip may be quite large without clearly increasing the fore drag over that of a sharp pointed cone of the same fineness ratio.

Cleary⁶ studied the flow of a perfect gas over a spherically blunted nose cone with 15° and 30° semi-cone angles with bluntness ratios of 6 and 5.45, at hypersonic Mach numbers, experimentally and theoretically. It was observed that at 0° angle of attack, the measured pressure distributions compare reasonably well with the inviscid numerical calculations. Also, the predictions and measurement revealed the existence of a low total-pressure layer near the blunted cone surfaces, surrounded by a high total-pressure layer. He noticed that the high total-pressure layer is due to the inflection of shock, which indicates the

three-dimensional characteristics of the flow past blunted nose cones.

Heberle et al.⁷ experimentally studied the form and the position of the detached shock waves on cones and spheres for the range of Mach numbers from 1.17 to 1.81 and the semi-cone angles between 35° and 90° . The measurements of the shock waves were done using a series of interferograms taken for the flow around cones and spheres and the data obtained were correlated to find the equations that explain the section of the shock wave in front of the sonic line. The data obtained at the boundaries of the subsonic region behind the detached shock wave was used to determine the pressure distribution and drag on the fore section of cones and spheres.

Saravanan et al.⁸ experimentally studied the surface convective heating rate on a missile-shaped body with and without fins in a hypersonic shock tunnel at a stagnation enthalpy of 2 MJ/kg and zero angle of attack. The experiments were performed at Mach numbers of 5.75 and 8 with an effective time of 1 ms. They observed that the heat transfer data measured at the stagnation point matches well with those determined using Fay and Riddell.⁹ It is also observed that the heat transfer rate achieved with fins is slightly higher than that of the model without fins.

1.1 Objectives of the present work

The schematics of the flow past spherically blunted and parabolic nose cones showing bow shock near the nose, shock layer, shock detachment distance, etc., are depicted in Figure 1. This paper shows the flow/shock characteristics, such as aerodynamic drag, shock detachment distance, location and shape of the bow shock, and attached shock formed ahead of the different nose cones at zero angle of attack near the nose cones. The modification in the flow/shock structures, which plays a vital role in enhancing the drag and heat flux reductions, finds numerous applications in the design of high speed aerodynamic vehicles. The studies are performed on two different nose cone geometries, namely spherically blunted and parabolic nose cones with different fineness ratios (L/D) at zero angle of attack in order to determine the effect of the geometry and parameters on the flow/shock (i.e., aerodynamic) characteristics. The schematics of the blunted and parabolic nose cones for different fineness ratios are shown in Figure 2. The physical differences in flow/shock characteristics of the different geometries are systematically compared using velocity vectors, Mach number contours, shock detachment distance, heat flux, etc. The effect of different nose cone geometries and parameters that provide minimum total aerodynamic drag for achieving better performance is also investigated. An empirical correlation for the total drag as a function of the maximum pressure coefficient

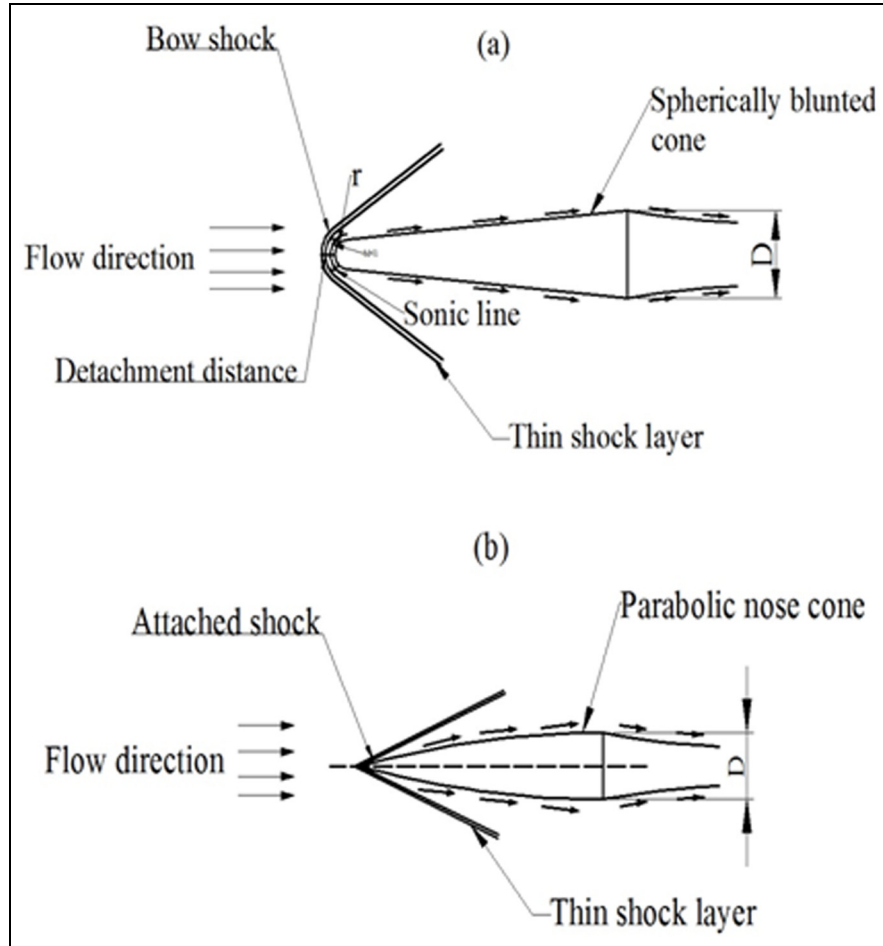


Figure 1. Schematic of flow field around (a) spherically blunted (b) parabolic nose cones.

and fineness ratio is developed for parabolic nose cones using regression analysis. Further, the aerodynamic heating effects of spherically blunted and parabolic nose cones are compared to determine the geometry that provides minimum heating.

2. Numerical methodology

2.1 Governing equations

The two-dimensional (2D) steady axisymmetric governing equations, which govern the occurrence of the physical phenomena when there is a hypersonic flow past a nose cone, are as follows:

Mass conservation equation:

$$\frac{\partial}{\partial x}(\rho u_x) + \frac{1}{r} \frac{\partial}{\partial r}(\rho u_r) = 0 \quad (1)$$

where x is the axial coordinate, r is the radial coordinate, u_x is the axial velocity, and u_r is the radial velocity.

Momentum conservation equation (axial direction):

$$\begin{aligned} & \frac{1}{r} \frac{\partial}{\partial x}(r \rho u_x u_x) + \frac{1}{r} \frac{\partial}{\partial r}(r \rho u_r u_x) \\ &= -\frac{\partial p}{\partial x} + \frac{1}{r} \frac{\partial}{\partial x} \left[r \mu \left(2 \frac{\partial u_x}{\partial x} - \frac{2}{3} (\nabla \cdot \vec{u}) \right) \right] \\ &+ \frac{1}{r} \frac{\partial}{\partial r} \left[r \mu \left(\frac{\partial u_x}{\partial r} + \frac{\partial u_r}{\partial x} \right) \right] + F_x \end{aligned} \quad (2)$$

Momentum conservation equation (radial direction):

$$\begin{aligned} & \frac{1}{r} \frac{\partial}{\partial x}(r \rho u_x u_r) + \frac{1}{r} \frac{\partial}{\partial r}(r \rho u_r u_r) \\ &= -\frac{\partial p}{\partial r} + \frac{1}{r} \frac{\partial}{\partial x} \left[r \mu \left(\frac{\partial u_r}{\partial x} + \frac{\partial u_x}{\partial r} \right) \right] \\ &+ \frac{1}{r} \frac{\partial}{\partial r} \left[r \mu \left(2 \frac{\partial u_r}{\partial r} - \frac{2}{3} (\nabla \cdot \vec{u}) \right) \right] \\ &- 2 \mu \frac{u_r}{r^2} + \frac{2 \mu}{3 r} (\nabla \cdot \vec{u}) + \rho \frac{u_z^2}{r} + F_r \end{aligned} \quad (3)$$

where

$$\nabla \cdot \vec{u} = \frac{\partial u_x}{\partial x} + \frac{\partial u_r}{\partial r} + \frac{u_r}{r}$$

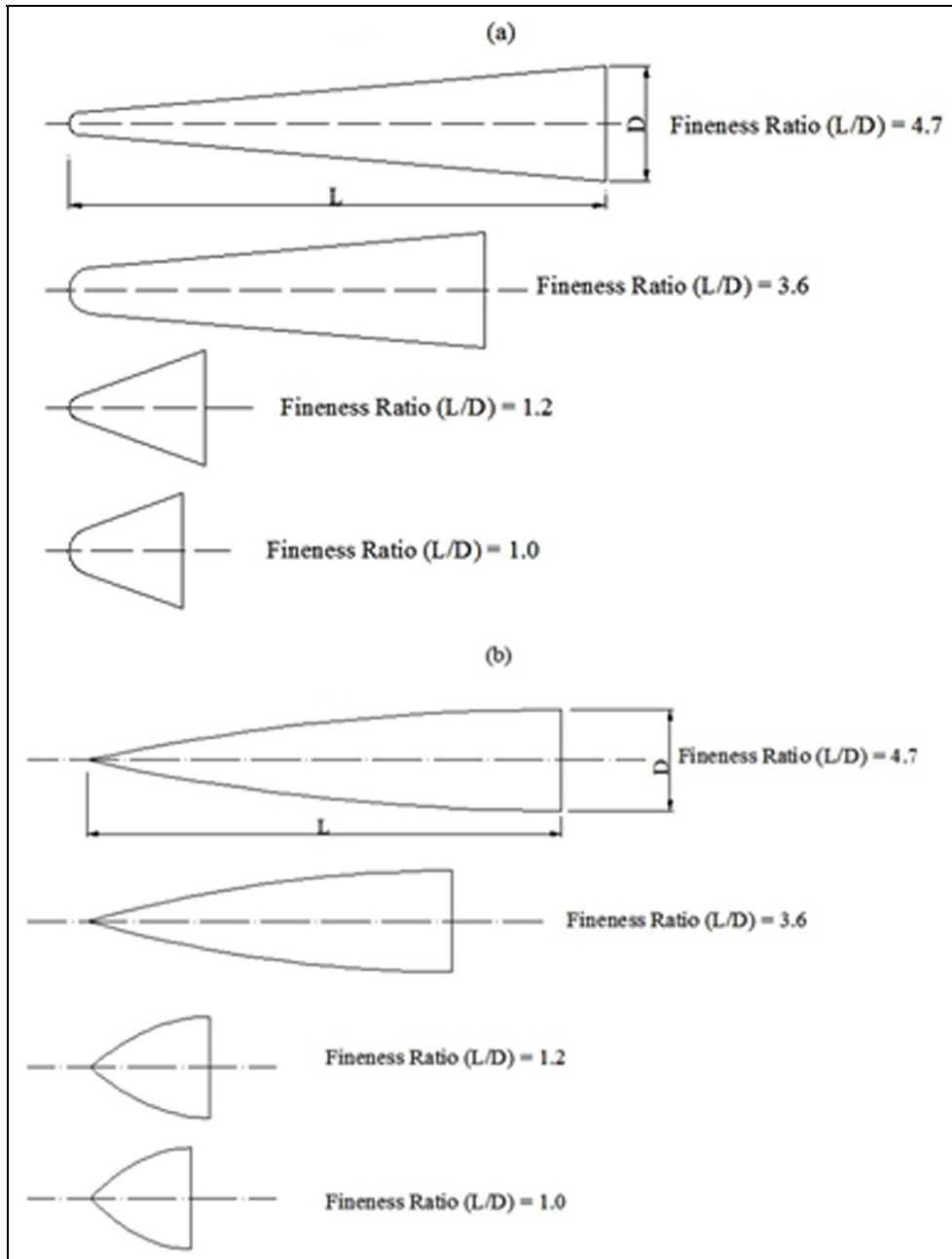


Figure 2. Detailed drawings of the (a) spherically blunted (b) parabolic nose cones geometries of different fineness ratio (L/D) combinations studied in the present simulation.

F_x and F_r comprise external body forces, model-dependent sources terms, and user-defined sources, and u_z is the swirl velocity.

Energy conservation equation:

$$\nabla \cdot (\vec{u}(\rho E + p)) = \nabla \cdot (k_{eff} \nabla T + (\bar{\tau}_{eff} \cdot \vec{u})) \quad (4)$$

where k_{eff} is the effective thermal conductivity ($k_{eff} = k + k_t$) and k_t is the turbulent thermal conductivity defined

based on the turbulence model. The first term on the right-hand side of Equation (4) represents energy transfer due to conduction, which is zero here due to adiabatic boundary conditions imposed on the cone surface, and the second term represents viscous dissipation.

Equation of state:

$$p = \rho R_c T \quad (5)$$

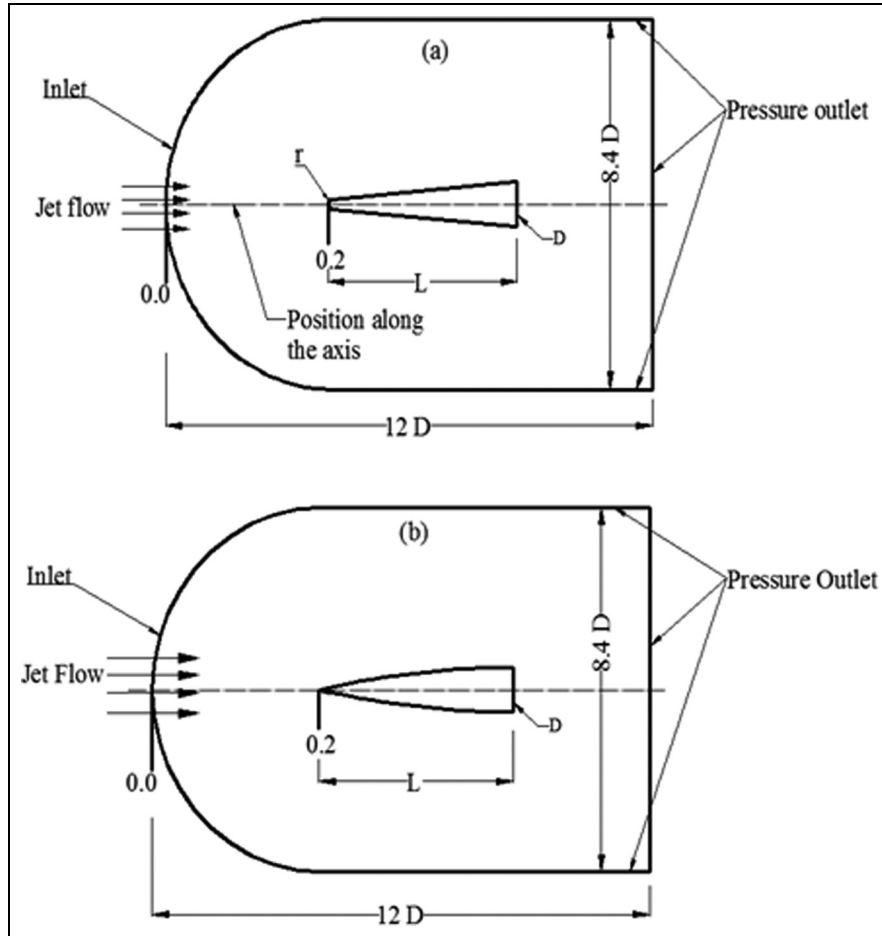


Figure 3. Computational domain and boundary conditions: (a) spherically blunted; (b) parabolic nose cone.

2.2 Solution method

2.2.1 Computational domain, boundary conditions, and grid. The computational domain and boundary conditions for the hypersonic flow past spherically blunted and parabolic nose cones are shown in Figure 3. The computational domain (Figure 3) is limited to 12 and 8.4 D in the axial and radial directions for predicting the complex flow/shock features, such as shock structures, recirculation zones, aerodynamic characteristics, etc., around the spherically blunted and parabolic nose cones for different nose cone geometries and parameters. The computational grid with varying mesh size, as shown in Figure 4, is constructed using ANSYS CFD software for predicting the complex flow/shock features when there is hypersonic flow past spherically blunted and parabolic nose cones. Grids with numbers of cells varying from approximately 150,000 to 200,000 are generated for different fineness ratios. The grids are made fine in the shock dominated regions in order to capture the complex flow/shock structures and coarse where the flow effects are less.

The grid sensitivity studies are carried out by varying the number of cells as follows: 150,000, 175,000, and

200,000. The study revealed that the current results obtained with 150,000 cells for different L/D values 0.6, 0.8, 1.0, 1.2, 1.5, 2.6, 3.6, 4.7 are almost invariant to further grid refinement. The variation of static pressure with position along the axis for various grids is shown in Figure 5 at a fineness ratio of 4.7. The maximum wall y^+ value near the surface is restricted to about 4 in order to properly resolve the boundary layer near the cone surface. A steady axisymmetric simulation is carried out with an implicit density-based solver. The fluid is considered as ideal gas for the present simulations with no slip boundary condition imposed at the walls. The present study primarily focuses on investigating the aerodynamic characteristics of spherically blunted and parabolic nose cones of different parameters to determine the geometry and parameters for minimum drag in order to augment the aerodynamic performance (i.e., efficiency) in hypersonic vehicles.

2.2.2 Turbulence model. The turbulence in the current simulation is modeled using the one-equation Spalart–Allmaras model with standard values of model constants ($\sigma_\nu = 2/3$, $C_{b1} = 0.1355$, $C_{b2} = 0.622$, $k = 0.42$, $C_{w1} = 3.21$, $C_{w2} = 0.3$,

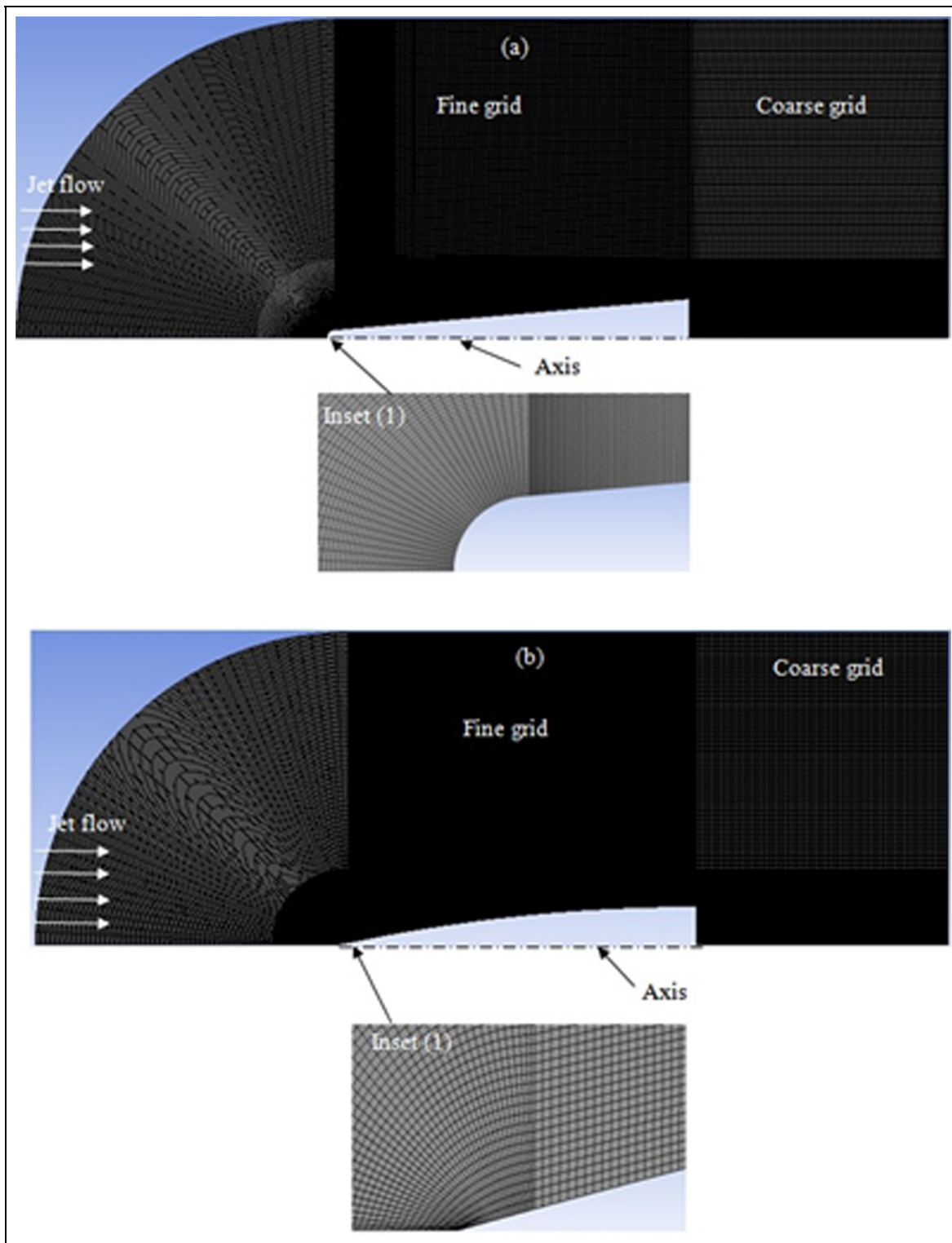


Figure 4. Computational grid: enlarged view of the grid near the (a) spherically blunted and (b) parabolic nose cones.

$C_{w3} = 2.0$, $C_{\nu 1} = 7.1$). The Spalart–Allmaras turbulence model is a fairly simple one-equation model that solves a modeled transport equation for the kinematic eddy

(turbulent) viscosity near the wall. Further, this simple one-equation model has been seen to provide good results with reduced computational time for problems involving

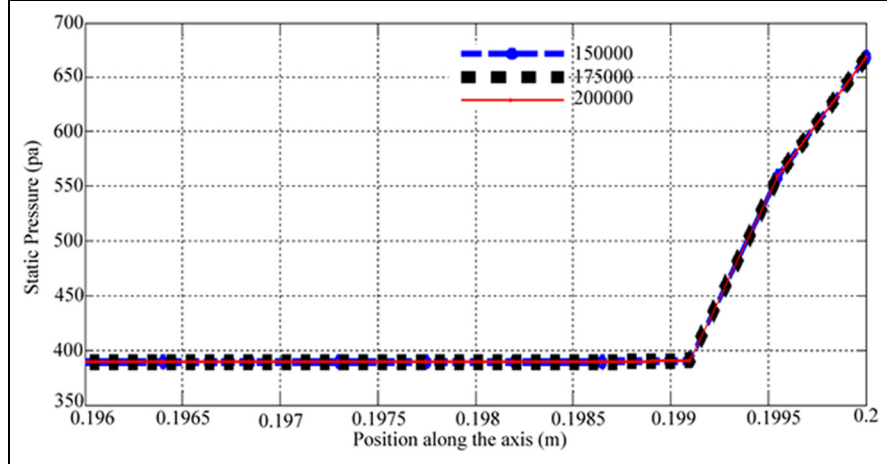


Figure 5. Axial variation of static pressure of a parabolic nose cone (fineness ratio = 4.7) for various grids showing grid sensitivity.

wall bounded flows as well as boundary layers subjected to adverse pressure gradients.¹⁰ Also, the Spalart–Allmaras model has been implemented to use wall functions when the mesh resolution is not sufficiently fine and, hence, it can be the finest choice for doing relatively rough simulations on coarse meshes where accurate turbulent flow computations are not crucial.

The transported variable in the Spalart–Allmaras model is equivalent to the turbulent kinematic viscosity (i.e., kinematic eddy viscosity) except in the viscous-affected (near-wall) region. The transport equation for $\tilde{\nu}$ is given by the following:

$$\frac{\partial}{\partial t}(\rho\tilde{\nu}) + \frac{\partial}{\partial x_i}(\rho\tilde{\nu}u_i) = G_v + \frac{1}{\sigma_{\tilde{\nu}}} \left\{ \frac{\partial}{\partial x_i} \left[(\mu + \rho\tilde{\nu}) \frac{\partial \tilde{\nu}}{\partial x_j} \right] + C_{b2}\rho \left(\frac{\partial \tilde{\nu}}{\partial x_i} \right)^2 \right\} - Y_v + S_{\tilde{\nu}} \quad (6)$$

where G_v is the generation of the turbulent viscosity and Y_v is the destruction of the eddy viscosity in the near-wall region due to viscous damping and wall blocking, $\sigma_{\tilde{\nu}}$ and C_{b2} are the constants and ν is the molecular kinematic viscosity, and $S_{\tilde{\nu}}$ is the user-defined source term, which is zero in the present simulation:

$$\mu_t = \rho\tilde{\nu}f_{\nu 1} \quad (7)$$

where $f_{\nu 1}$ is the viscous damping function and is given as $f_{\nu 1} = \frac{\chi^3}{\chi^3 + C_{\nu 1}^3}$ and $\chi = \frac{\tilde{\nu}}{\nu}$.

The generation term G_v is modeled as follows:

$$G_v = C_{b1}\rho\tilde{\nu} \left(S + \frac{\tilde{\nu}}{k^2 d^2} \left(1 - \frac{\chi}{1 + \chi f_{\nu 1}} \right) \right) \quad (8)$$

where C_{b1} and k are constants, d is the distance from the wall, and S is the scalar measure of the deformation tensor based on the magnitude of vorticity, given as $S = \sqrt{2\Omega_{ij}\Omega_{ij}}$, where Ω_{ij} is the mean rate of the rotation tensor defined by $\Omega_{ij} = 0.5 \left(\frac{\partial u_i}{\partial x_j} - \frac{\partial u_j}{\partial x_i} \right)$.

The destruction term is modeled as follows:

$$Y_v = C_{w1}\rho \left(\frac{\tilde{\nu}}{d} \right)^2 \left(g \left[\frac{1 + c_{w3}^6}{g^6 + c_{w3}^6} \right]^{1/6} \right) \quad (9)$$

where

$$g = \frac{\tilde{\nu}}{Sk^2 d^2 + \tilde{\nu} \left(1 - \frac{\chi}{1 + \chi f_{\nu 1}} \right)} + C_{w2} \left[\left(\frac{\tilde{\nu}}{Sk^2 d^2 + \tilde{\nu} \left(1 - \frac{\chi}{1 + \chi f_{\nu 1}} \right)} \right)^6 - \frac{\tilde{\nu}}{Sk^2 d^2 + \tilde{\nu} \left(1 - \frac{\chi}{1 + \chi f_{\nu 1}} \right)} \right] \quad (10)$$

and $\sigma_{\tilde{\nu}}$, C_{b1} , C_{b2} , k , C_{w1} , C_{w2} , C_{w3} , $C_{\nu 1}$ are the model constants whose standard values are mentioned above.

3. Validation

3.1 Comparison of shock detachment distance obtained from the current predictions with the theory for spherically blunted nose cones

To ensure our numerical predictions are correct, the shock detachment distance, as shown in Figure 6(a), of spherically blunted nose cones for different fineness ratios obtained from the present simulations are compared with the theory.¹ It is noticed that the predicted and the theoretical shock detachment distance shows decreasing trend

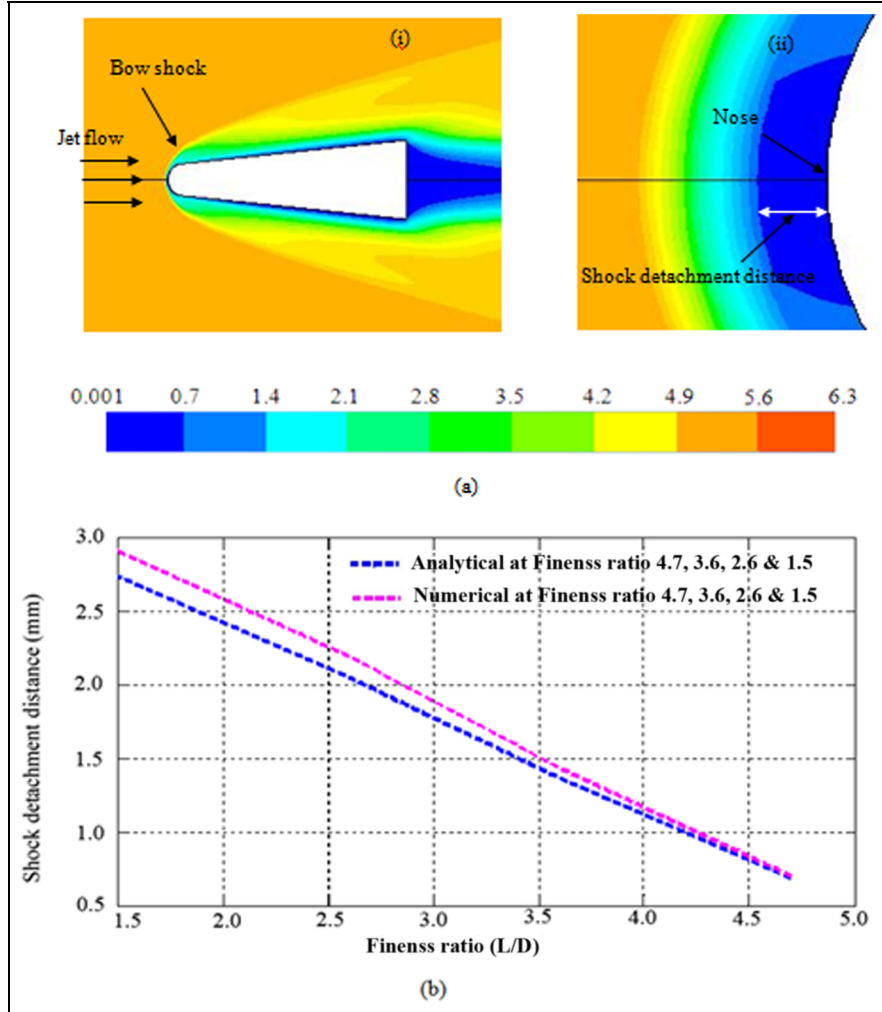


Figure 6. (a) Mach number contour showing shock detachment distance. (b) Comparison of shock detachment distance with L/D between theory and the prediction of a spherically blunted nose cone at 4.7, 3.6, 2.6, 1.5.

with fineness ratios, as shown in Figure 6(b). At small fineness ratios the deviation between the predicted detachment distance and those obtained from the theory is within about 5%, whereas at higher fineness ratios the deviation is almost negligible. In general, the shock detachment distance obtained from predictions shows good agreement with the theory (Equation (11)) given by O'Bryant¹ (i.e., about 5%):

$$\frac{\delta}{r} = \frac{1}{\rho_x/\rho_y \left(1 - \sqrt{1 - \left(1 - \rho_x/\rho_y \right)^2} \right)} - 1 \quad (11)$$

where δ is the shock detachment distance, mm, r is the nose radius, mm, and ρ_x/ρ_y is the density ratio before and after the strong shock:

$$\frac{\rho_x}{\rho_y} = \frac{\left(1 + \frac{\gamma - 1}{2} M_\infty^2 \right)}{\frac{\gamma + 1}{2} M_\infty^2} \quad (12)$$

4. Results and discussion

4.1 Numerical predictions of flow around spherically blunted and parabolic nose cones

4.1.1 Comparison of Mach number contours of spherically blunted and parabolic nose cones for different fineness ratios. The comparison of Mach number contours of spherically blunted and parabolic nose cones for various fineness ratios (a) 4.7 (b) 3.6 (c) 1.2, and (d) 1.0 is shown in Figure 7 in order to determine the modifications in the flow/shock structures due to modifications in the nose cone geometries. The bow shock is formed very close to the nose for the spherically blunted nose cone,

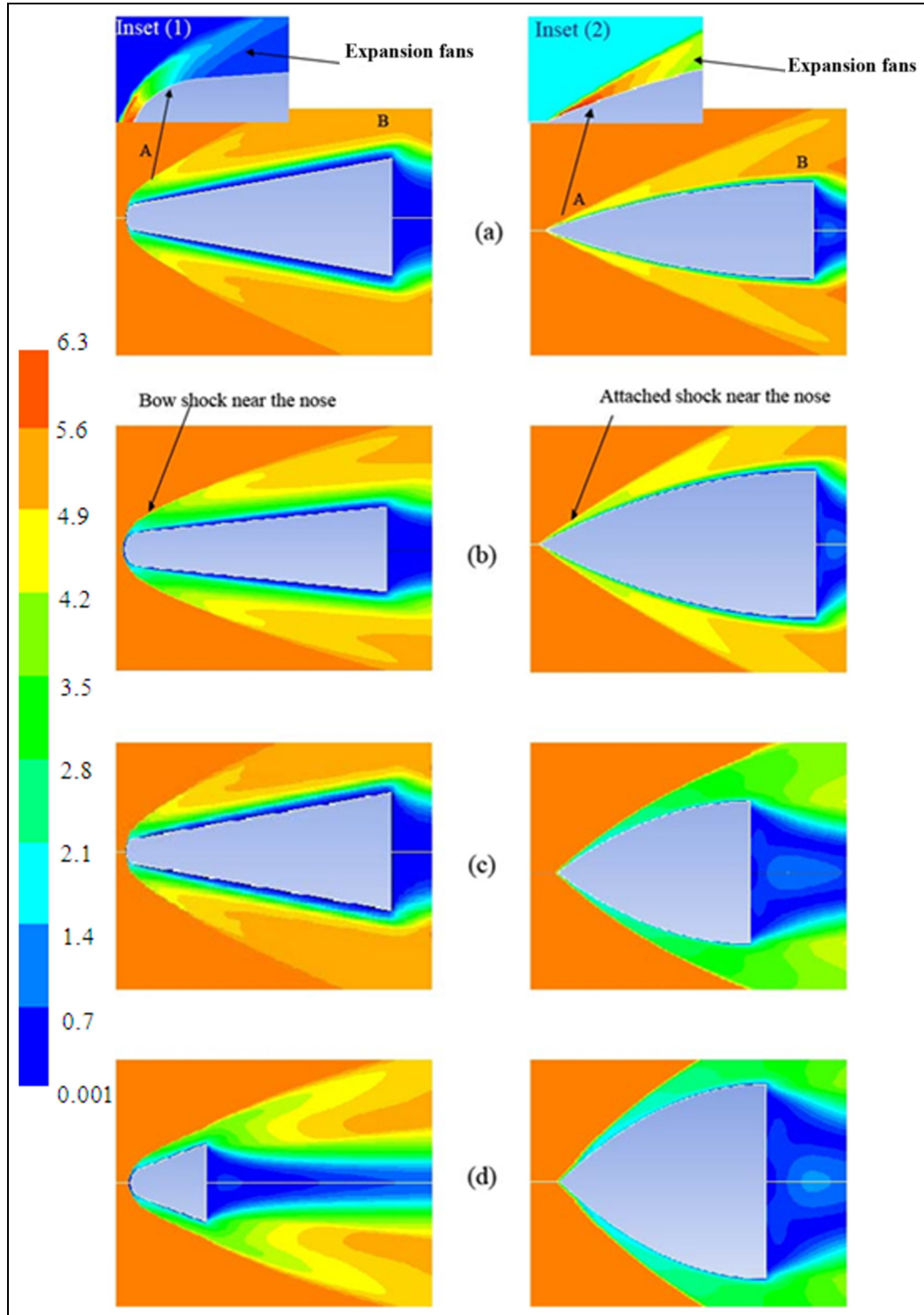


Figure 7. Comparison of Mach number contours of a spherically blunted nose cone and parabolic nose cones at various fineness ratios: (a) 4.7; (b) 3.6; (c) 1.2; (d) 1.0.

as shown on the left-hand side of Figure 7(a), and attached shock is formed near the parabolic nose cone, as shown on the right-hand side of Figure 7(a). The bow shock wave is normal to the flow direction near the nose

and the flow passes through it without turning and comes to rest when it reaches the nose. The shock wave is inclined to the flow direction (i.e., oblique) above and below the normal shock, as shown on the left-hand side

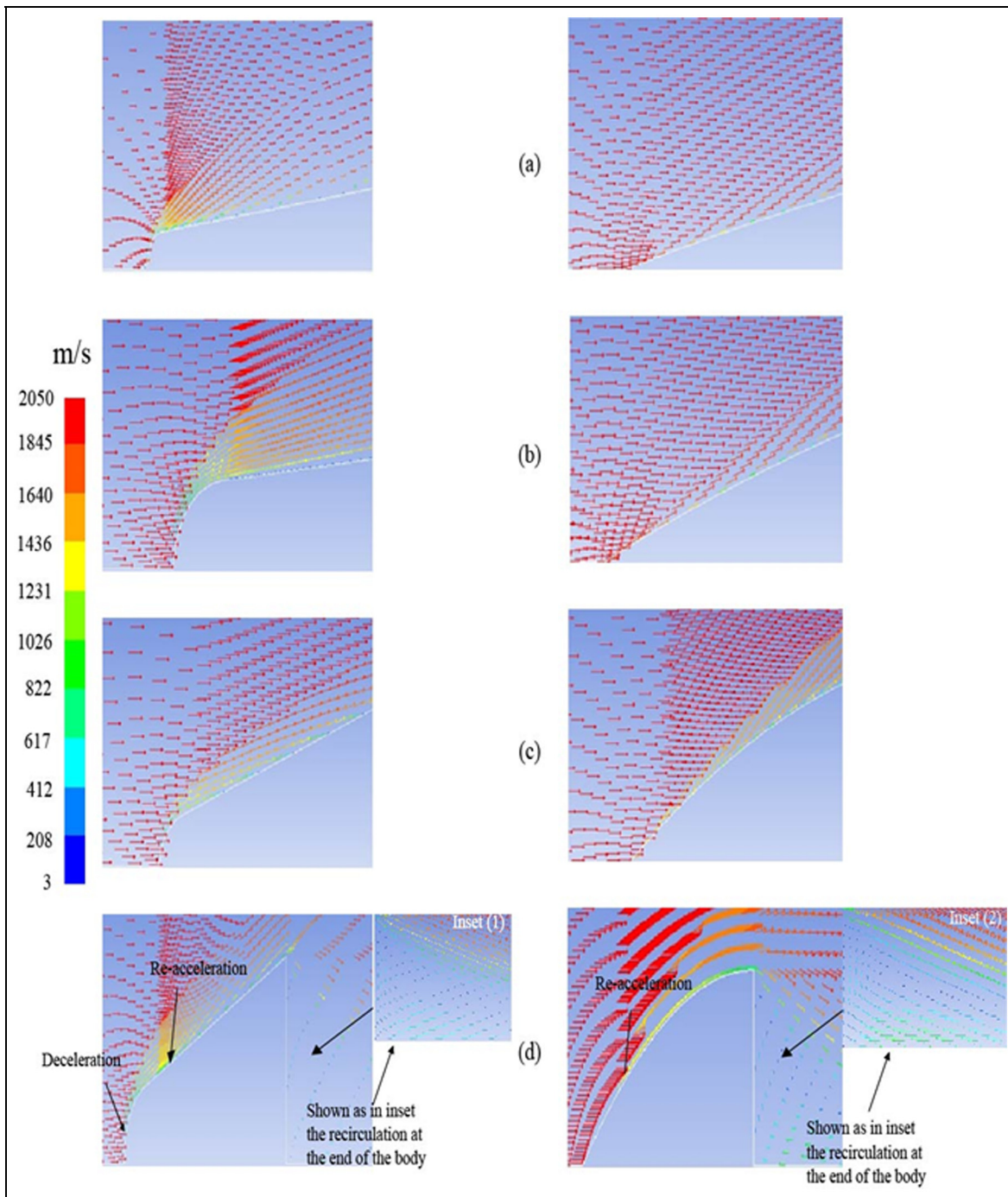


Figure 8. Comparison of velocity vector of a spherically blunted nose cone and parabolic nose cones at various fineness ratios: (a) 4.7; (b) 3.6; (c) 1.2; (d) 1.0.

of Figure 7(a), which turns the flow near the nose, but in the parabolic nose cone the shock wave is sharply inclined to the flow direction (i.e., oblique) above and below the leading edge of the nose, as shown on the right-hand side of Figure 7(a). The complete flow turning cannot be accomplished by oblique shock alone. Initially, the oblique shock turns the flow towards it and,

following that, the flow has to be turned in the opposite direction to move parallel to the nose cone surface, which is further accomplished by the formation series of expansion fans shown on the left-hand side as inset (1) in Figure 7(a), which turns the flow away from it and makes it parallel to the nose cone surface. As the flow reaches the cone base, the flow has to be turned

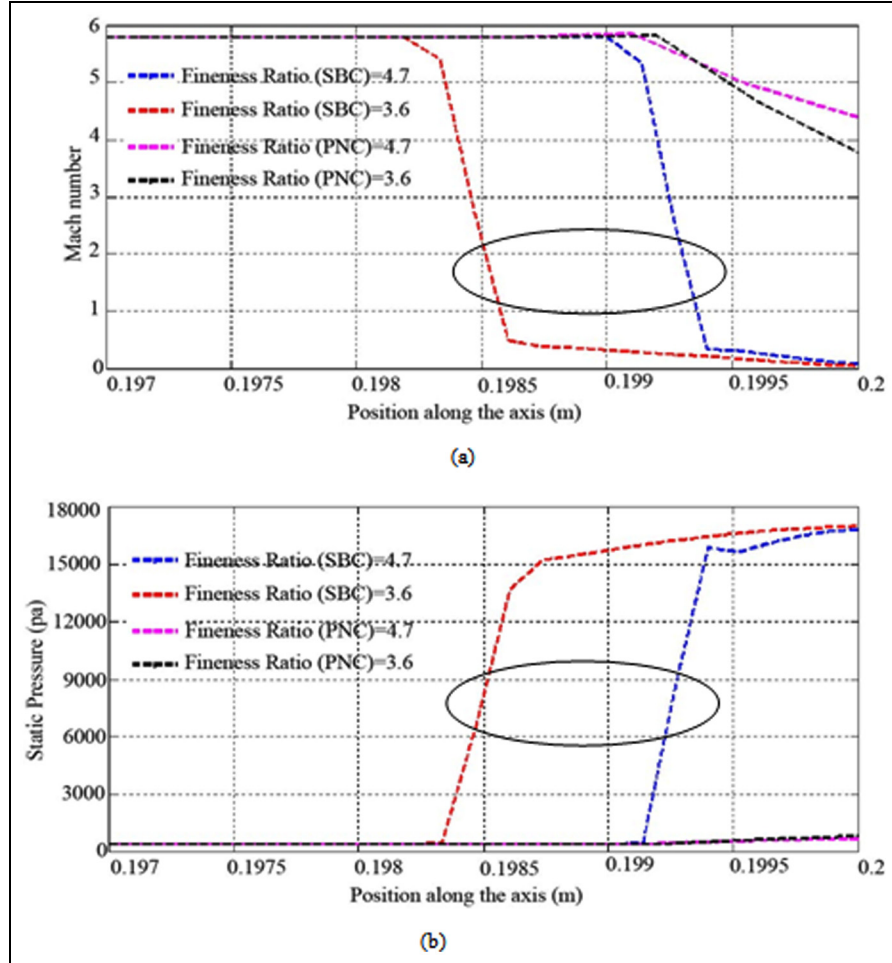


Figure 9. Comparative variation of (a) Mach number and (b) static pressure with position along the axis of a spherically blunted nose cone and parabolic nose cone at fineness ratios of 4.7 and 3.6.

downward to make it parallel to the axis, which is further accomplished by the series expansion fans formed near the cone base. In the parabolic nose cone, the flow turning is initially accomplished by an oblique shock wave and the expansion fan is not formed near the nose as seen in the spherically blunted nose cone, but the expansion fans following the oblique shock are formed near the location of the curved section shown on the right-hand side as inset (2) in Figure 7(a), which turns the flow away from it and makes it parallel to the nose cone surface and, at the cone base, the flow turning is similar to the spherically blunted nose cone. Decrease in the fineness ratio reduces the overall length of the nose cone and makes the cone broader. In this case, the flow turning near the nose is completely accomplished by the bow shock wave and the attached oblique shock wave instead of the combined effect of the oblique shock wave and the expansion fans, as seen in Figures 7(a) and (b), and the flow turning near the cone base is achieved through the formation of series of small expansion fans.

4.1.2 Comparison of the velocity vector of spherically blunted and parabolic nose cones for different fineness ratios. The steady-state velocity vectors of spherically blunted and parabolic nose cones are shown in Figure 8. It clearly depicts the flow features, such as deceleration near the nose, re-acceleration through the sideways of the cone, and recirculation zones. The hypersonic flow decelerates to subsonic near the nose due to the formation of strong normal shock, and thereafter it re-accelerates through the sideways and turns from a sonic line to supersonic through the oblique shock and series of expansion fans formed near the nose, as mentioned above. In the parabolic nose cone the flow decelerates near the location from the nose where the curvature in the geometry begins; thereafter, the flow reaccelerates sideways through the series of expansion fans following the oblique shock that is formed near the location of the curved section. In both the spherically blunted and parabolic nose cones a strong recirculation zone is observed behind the base, which represents the low-pressure and low-velocity wake zones in hypervelocity vehicles.

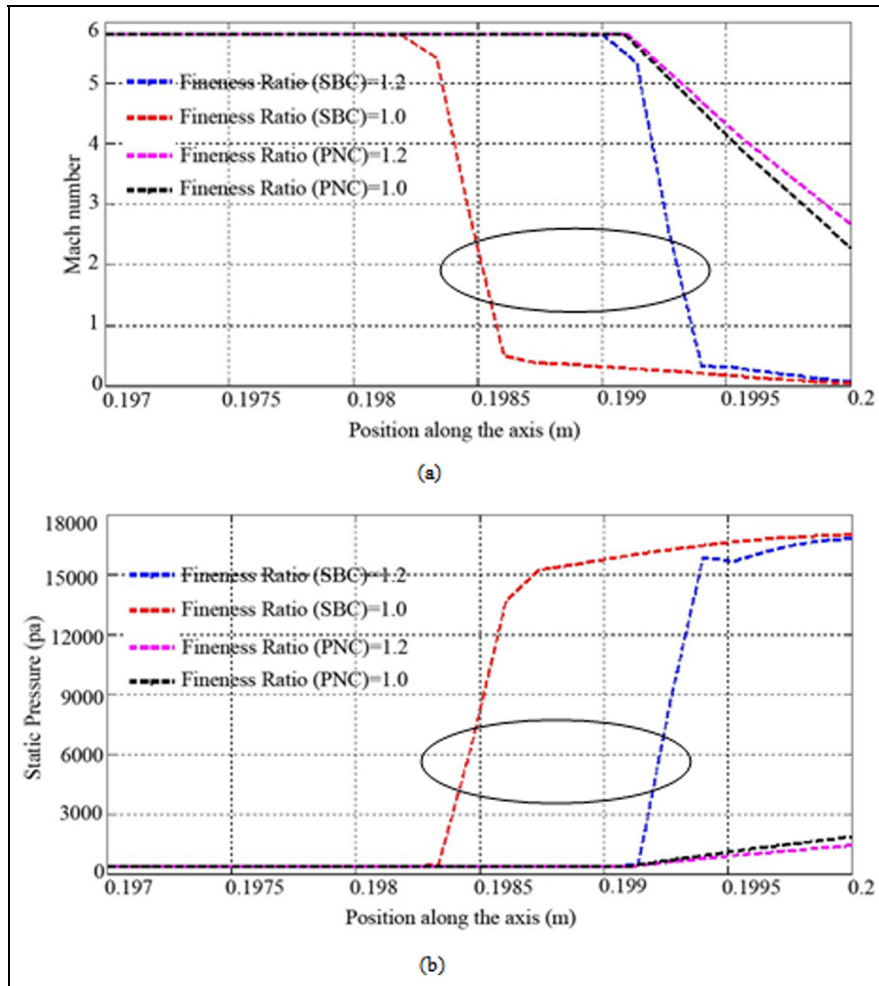


Figure 10. Comparative variation of (a) Mach number and (b) static pressure with position along the axis of a spherically blunted nose cone and parabolic nose cone at fineness ratios of 1.2 and 1.0.

4.1.3 Variation of Mach numbers and static pressure with position along the axis of spherically blunted and parabolic nose cones for various fineness ratios. The variation of Mach numbers and static pressure with position along the axis of spherically blunted and parabolic nose cones at various fineness ratios is shown in Figures 9 and 10. The location of the bow shock near the spherically blunted nose cone is represented by a sudden jump in the Mach number and static pressure plots, marked as an ellipse in Figures 9 and 10, whereas a small jump is observed in the case of parabolic nose cones. The distance between the nose cone surface and the normal component of the bow shock in spherically blunted nose cones is known as the shock detachment distance, which occurs as a sharp change in the slope of the Mach number and static pressure plots, as shown in Figures 9 and 10. In the case of the parabolic nose cone, due to the formation of attached shock near the nose cone the detachment distance is not present, as shown in Figures 9 and 10. The presence of very low static

pressure in the parabolic nose cone, as shown in Figures 9 and 10, may be the reason for the reduction of low drag as compared to the spherically blunted cone.

4.1.4 Comparison of pressure and total drag coefficient with fineness ratio for spherically blunted and parabolic nose cones. The variation of pressure drag with fineness ratios is shown in Figure 11(a). It is observed that the pressure drag coefficient decreases with increasing fineness ratio. The literature review shows that spherically blunted cones possess a higher drag coefficient as compared to parabolic nose cones, but the influence of fineness ratio on the aerodynamic drag is unknown. The present study reveals the existence of low aerodynamic drag in parabolic nose cones at higher fineness ratios (>1.2) (Figure 11(a)), whereas at lower fineness ratios (<1.2) (Figure 11(a)) spherically blunted cones offer superior performance over parabolic ones. Similar results are achieved for the total drag (i.e., pressure drag + viscous drag) also for both the spherically

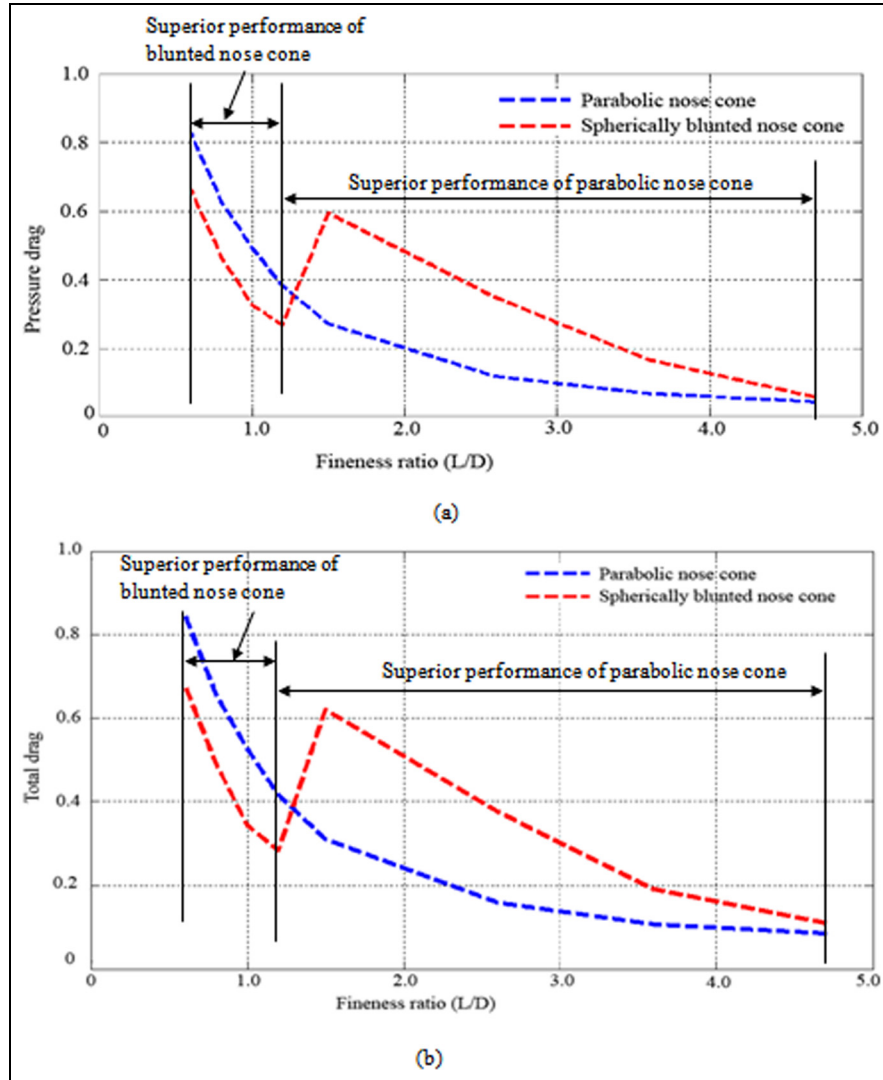


Figure 11. Comparison of (a) pressure drag and (b) total drag (i.e., pressure drag + viscous drag) of the parabolic nose cone and spherically blunted nose cone for different fineness ratios.

blunted and parabolic nose cones, as shown in Figure 11(b). The similar features of the pressure drag and total drag, as mentioned above, indicate that the effect of viscous drag on the performance enhancement is almost negligible. Thus, it shows that the parabolic nose cones with higher fineness ratio values are essential for achieving minimum drag in hypervelocity vehicles. Thus, the present study reveals that the existence of smaller aerodynamic drag in parabolic nose cones is due to the reduction of the maximum pressure coefficient, as compared to the spherically blunted cone as mentioned earlier.

4.1.5 Comparison of wall heat flux with fineness ratio for spherically blunted and parabolic nose cones. The comparison of heat flux variations with the position along the surface of both spherically blunted and parabolic nose cones

at higher fineness ratios (4.7 and 3.6) is shown in Figure 12(a). It is noticed that heat flux decreases rapidly up to a certain distance along the wall and thereafter it remains almost constant, for both nose cone geometries studied. Similar features are observed for lower fineness ratios (1.2 and 1.0), as shown in Figure 12(b). The reason for the higher heat flux observed near the nose may be due to the stagnation point, which decays further downstream, and the surface heat flux distribution, which approaches the inviscid value far downstream from the nose. In general, it is noticed that the surface heat flux along the parabolic nose cone is lower as compared to spherically blunted ones. This may be due to the modifications in the flow/shock structures near the nose cone surface due to the complex shock-boundary layer interaction; however, the exact reason for this behavior is still unclear.

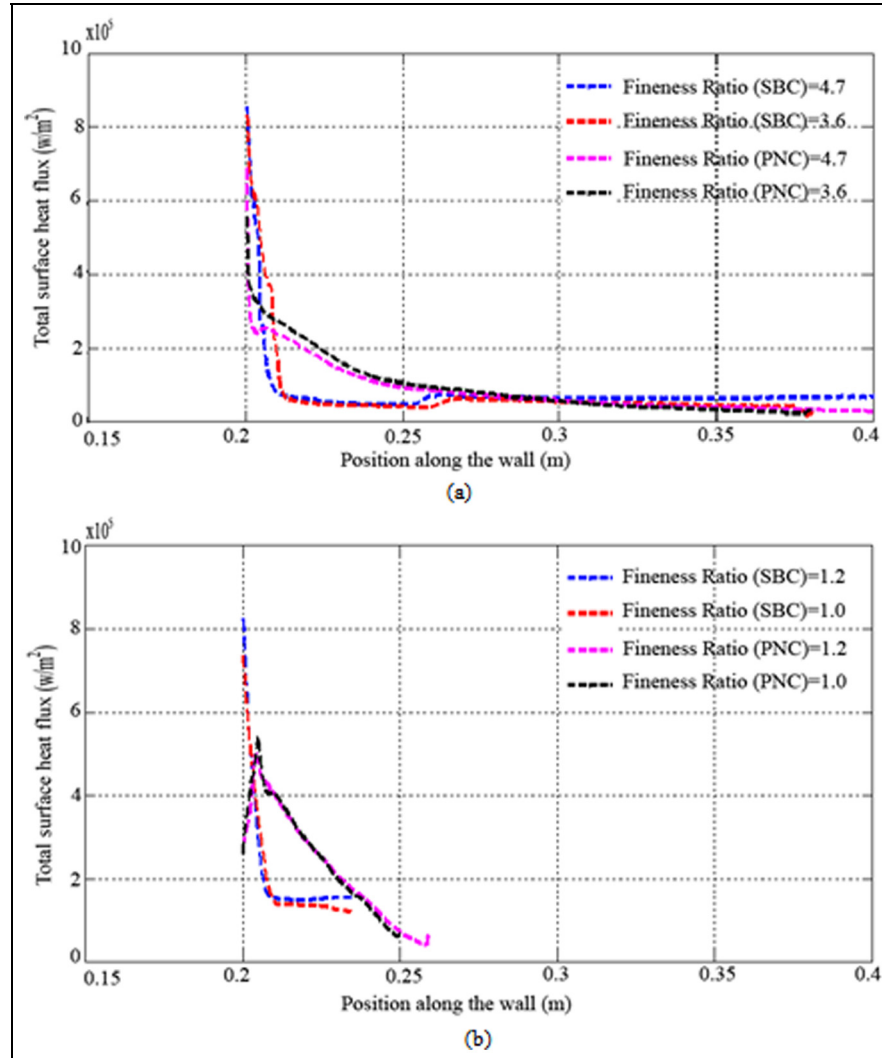


Figure 12. Variation of total surface heat flux with position along the wall of spherically blunted and parabolic nose cones at fineness ratios of (a) 4.7 and 3.6 and (b) 1.2 and 1.0.

4.1.6 Development of an empirical correlation for the drag coefficient in parabolic nose cones. The color map, as shown in Figure 13(a), reveals that value of C_d attains maximum at smaller L/D values, whereas at higher L/D values C_d decreases to a smaller value. From this it is clear that the prominent parameters influencing the drag coefficient of the parabolic nose cones are the maximum pressure coefficient ($C_{p\max}$) and fineness ratios (L/D). Thus, the dimensionless drag coefficient C_d must be a function of $C_{p\max}$ and L/D , which can be mathematically expressed as follows:

$$C_d = f(C_{p\max}, L/D) \quad (13)$$

The dimensionless drag C_d when plotted against the non-dimensional parameters, such as $C_{p\max}$ and L/D , could provide an equation for the estimation of the drag coefficient in parabolic nose cones. The regression analysis performed

on this data revealed that the predicted drag coefficient (Figure 13(b)) matches very well to those obtained numerically with a correlation factor r_c greater than 0.99, thus following a linearly increasing behavior. Thus, an empirical correlation is developed in the present study to determine the total drag coefficient in parabolic nose cones, which is given as follows:

$$C_d = C_{p\max} [0.248X(L/D) + 0.4061] \quad (14)$$

5. Conclusions

A detailed computational study of the hypersonic flow past spherically blunted and parabolic nose cones of different configurations and parameters is carried out to understand the flow/shock features, such as shock detachment

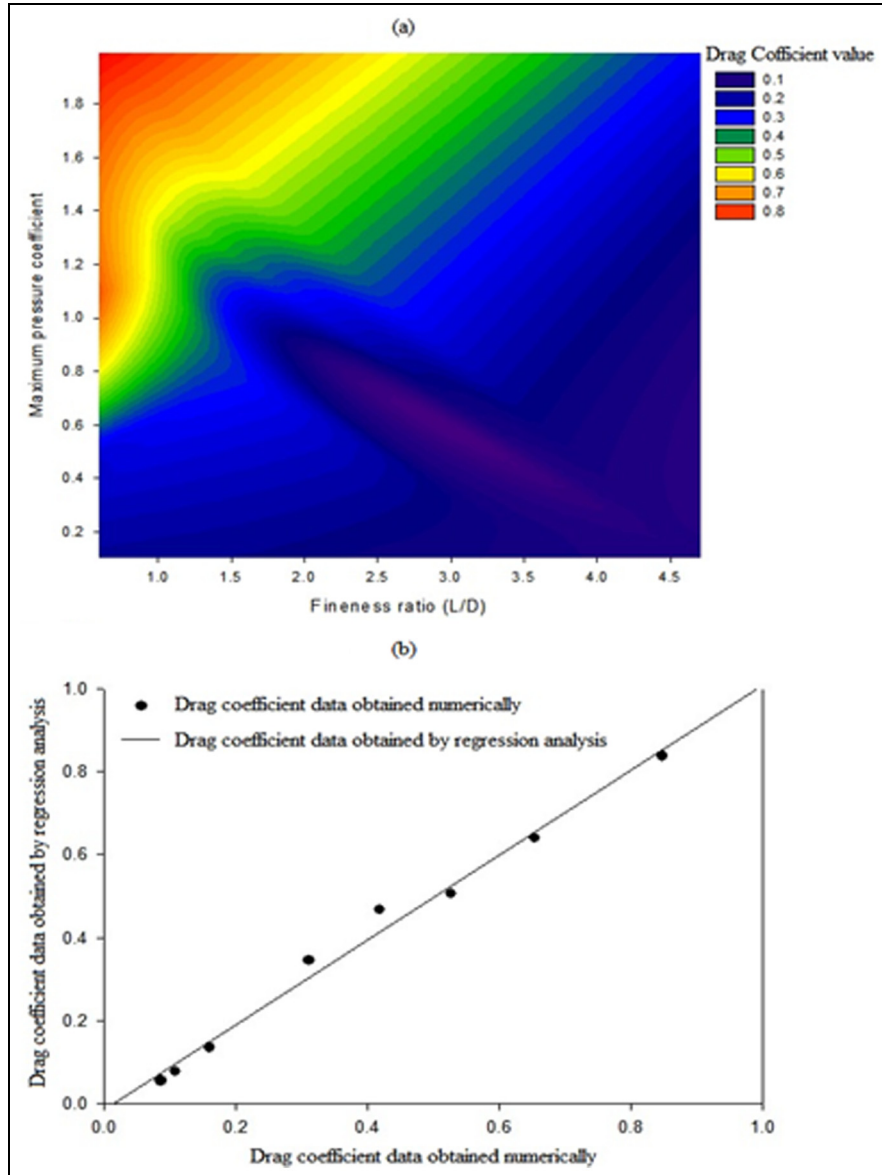


Figure 13. (a) Color map showing the variation of total drag coefficient with the maximum pressure coefficient and fineness ratio of parabolic nose cones. (b) Comparison of the drag coefficient obtained numerically with those predicted using regression analysis. (Color online only.)

distance, aerodynamic drag, heat flux, etc., and hence to determine the nose cone geometry that provides minimum aerodynamic drag and heating. The studies are conducted for various combinations of fineness ratios (0.6, 0.8, 1.0, 1.2, 1.5, 2.6, 3.6, 4.7) to determine the effect of fineness ratios on the aerodynamic characteristics.

The Mach number contours of a spherically blunted nose cone clearly show the structure of bow shock formed near the nose, which comprises strong and weak regions of flow separated by a sonic line through which flow re-accelerates to the supersonic velocity. Due to the presence of strong and thin normal shock that forms near the blunted

nose, the flow suddenly decelerates from the hypersonic range to the subsonic range. The velocity vector obtained from the present simulation shows the flow direction showing deceleration in front of the blunted nose followed by re-acceleration through the sideways of the nose cone, as mentioned above. The corresponding shock locations ahead of the blunted nose cones are indicated by the sudden jump in Mach number and static pressure plots with large gradients are marked as an ellipse. However, in the parabolic nose cone due to the formation of attached shock the sudden jump is not observed; instead, small jumps with weak gradients are seen in the Mach number and static

pressure plots. The existence of low aerodynamic drag in parabolic nose cones at higher fineness ratios (>1.2) indicates its superior performance over spherically blunted ones, which are better only for smaller fineness ratios (<1.2). The heat flux variation of the spherically blunted and parabolic nose cones decreases rapidly along the surface up to a certain distance along the wall and, thereafter, it remains almost constant. In general, it is observed that the heat flux is less in parabolic nose cones as compared to spherically blunted ones for all fineness ratios studied. An empirical correlation developed for the total drag coefficient based on regression analysis for parabolic nose cones reveals that it is mainly a function of the maximum pressure coefficient and fineness ratio. Thus, the present study reveals that parabolic nose cones at higher fineness ratios are preferred over spherically blunted ones for achieving higher drag reductions and lower heating in hypersonic vehicles.

Funding

This research received no specific grant from any funding agency in the public, commercial, or not-for-profit sectors.

References

- O'Bryant WT. *An experimental investigation of hypersonic flow over blunt nosed cone at Mach number of 5.8*. Thesis, California Institute of Technology, 15 June 1956.
- Menezes V, Kumar S, Maruta K, et al. Hypersonic flow over a multi-step afterbody. *Shock Waves* 2005; 14: 421–424.
- Arsalan MS, Husain M and Qureshi MN. Effects of nose-bluntness ratio on aerodynamic performance for re-entry vehicle. *J Space Technol* 2012; 1, pp. 38–41.
- Owens RV. *Aerodynamic characteristics of spherically blunted cones at mach numbers from 0.5 to 5.0*. Washington, DC: National Aeronautics and Space Administration, 1965.
- Perkins EW, Jorgensen LH and Sommer SC. Investigation of the drag of various axially symmetric nose shapes of fineness ratio 3 for mach numbers from 1.24 to 7.4. NACA Research Memorandum, 1952.
- Cleary JW. *An experimental and theoretical investigation of the pressure distribution and flow fields of blunted cones at hypersonic Mach numbers*. Washington, DC: National Aeronautics and Space Administration, 1965.
- Heberle JW, Wood GP and Gooderum PB. *Data on shape and location of detached shock waves on cones and spheres*. NACA TN 2000. Washington, DC: National Aeronautics and Space Administration, January 1950.
- Saravanan S, Jagadeesh G and Reddy KPJ. Convective heat-transfer rate distributions over a missile shaped body flying at hypersonic speeds. *Exp Therm Fluid Sci* 2009; 33: 782–790.
- Fay JA and Riddell FR. Theory of stagnation point heat transfer in dissociated air. *J Aeronaut Sci* 1958; 25: 73–85.
- Spalart PR and Allmaras SR. A one-equation turbulence model for aerodynamic flows. AIAA-92-0439. American Institute of Aeronautics and Astronautics, 1992.

Author biographies

Ashish Narayan received a Bachelor's degree from the Maharana Pratap College of Technology, Gwalior, RGPV Bhopal, Madhya Pradesh, India and received a M.Tech degree from BIT,Sindri, VBU, Hazaribagh, Jharkhand, India. He is a research scholar at the Mechanical Engineering Department in the Indian Institute of Technology (ISM), Dhanbad, Jharkhand, India. His research interest is focused on the design of hypervelocity vehicles, Turbulent flow.

Dr. S Narayanan is an Assistant Professor in the Department of Mechanical Engineering, IIT(ISM), Dhanbad. He received his PhD degree in Mechanical Engineering from IIT Madras in 2011. His main research interests comprise Shock-dominated flows, Turbulent flows, Aero-acoustics, Aerodynamics etc.

Dr. Rakesh Kumar is an Assistant Professor in the Department of Mechanical Engineering, IIT(ISM), Dhanbad. He received his PhD degree in Mechanical Engineering from IIT Guwahati in 2014. The author is doing research work with PhD and M.Tech students on the Development of various types of Resistance Temperature Detector (RTD) Sensors, Transient Temperature and Heat Flux Measurement Analysis in Microseconds or Nanoseconds, Internal Combustion Engine, Nanomaterials and Nanofluids.

Appendix

Nomenclature

- C_{dp} = Coefficient of pressure drag
 C_d = Total drag coefficient
 $C_{P\max}$ = Maximum pressure coefficient
 M_∞ = Free stream Mach number
 r = Nose radius, m
 D = Cone base diameter, m
 L = Length of the nose cone, m
 L/D = Fineness ratio
PNC = Parabolic nose cone
SBC = Spherically blunted nose cone
 δ = Shock detachment distance, m